Received: 16 January 2019 | Revised: 24 June 2019 | Accepted: 8 October 2019
DOI: 10.1002/we.2437

WILEY

RESEARCH ARTICLE

Power generation control of a hydrostatic wind turbine implemented by model-free adaptive control scheme

Shuyue Lin | **Pengyuan Qi** | **Xiaowei Zhao**

School of Engineering, University of Warwick, Coventry, UK

Correspondence
Xiaowei Zhao, School of Engineering, University of Warwick, Coventry CV4 7AL, UK.
Email: xiaowei.zhao@warwick.ac.uk

Funding information
Engineering and Physical Sciences Research Council, Grant/Award Number: EP/R015120/1

Abstract

The hydrostatic wind turbine (HWT) is a type of wind turbine that uses hydrostatic transmission (HST) drivetrain to replace the traditional gearbox drivetrain. Without the fragile and expensive gearbox and power converters, HWT can potentially reduce the maintenance costs owing to the gearbox and power converter failures in wind power system, especially in offshore cases. We design an MFAC torque controller to regulate the pump torque of the HWT and compared with an $\mathcal{H}_\infty$ torque controller. Then we design an MFAC pitch controller to stabilise the rotor speed of HWT and compared with a gain-scheduling proportional-integral (PI) controller and a gain-scheduling PI controller with antiwindup (PIAW). The results indicate that MFAC torque controller provides more effective tracking performance than the $\mathcal{H}_\infty$ controller and that MFAC pitch controller shows better rotor speed stabilisation performance in comparison with the gain-scheduling PI controller and PIAW.

KEYWORDS

hydrostatic wind turbine (HWT), model-free adaptive control (MFAC), power generation control

1 | INTRODUCTION

Fuel energy is believed to be the main contributor to global warming and air pollution. To deal with threats posed by environmental issues, there have been great improvements in renewable energy technologies.[1,2] As one of the most mature renewable energy technologies, wind power generation has witnessed a sustained and rapid development in recent years, becoming a preferable solution for greenhouse gas emission reductions in power generation industries. However, the uncontrollable nature of wind brings huge burdens to the wind turbine gearbox drivetrain under wind gusts, which is considered as a major cause for premature failure of wind turbines.[3-5] Particularly in the offshore cases, wind speed is faster, which further shortens the gearbox life expectancy and increases the wind turbine maintenance costs,[5-7] thus hindering the development of offshore wind power generation. Applying the multipole permanent magnetic synchronous generator (PMSG) direct-drive structure is capable of removing the vulnerable gearbox,[8,9] but it brings new problems of heavy nacelle and high costs because of the rare earths permanent magnetic materials.[9] It also requires full power converter connection for grid integration, which is known as another main factor for high maintenance costs.[5-7] In addition, the existence of power converters decouples the generator from the grid, which impedes the direct inertia response to the grid, leading to reduced system stability and reliability.[10]

Hydrostatic wind turbine (HWT) has the potential to address the above problems. HWT is a type of wind turbine that uses hydrostatic transmission (HST) drivetrain for power transmission between the wind turbine rotor and the generator. The HST is potentially more reliable than the traditional gearbox drivetrain.[4,5] The model usually includes a hydraulic pump, which is mechanically connected to the wind turbine rotor, as well as a hydraulic motor driven by the pump through pressurised fluid, which provides a damping effect reducing the stress to the generator. With proper control, the HWT can realise "continuously variable gearbox ratio," which means that it is allowed to connect to the synchronous generator (SG) and then directly to the grid without power converters. In this manner, gearbox and power converters can be removed, which could potentially reduce the maintenance costs relating to the gearbox and power converter failures and increase the power system reliability through direct inertia response to the grid.

In this paper, we will investigate the power generation control of the HWT. Similar to the conventional wind turbine, the power generation control is divided into four operation regions. When wind turbine operates in region 1 (below the cut-in speed) or region 4 (above the cut-out speed), no power is generated. In this study, we are only interested in the power generation control in region 2 and region 3, which mainly includes the torque control and pitch control. When the wind speed is above the cut-in speed and below the rated speed (ie, the wind turbine rotor starts operating with a speed lower than its rating), the wind turbine operates in region 2, and the power capture is optimised by torque control. When the wind speed is above the rated speed and below the cut-out speed (ie, the wind turbine rotor speed reaches its rating), the wind turbine operates in region 3, and the power extraction should be maintained at its rating by the cooperation between torque control and pitch control.[11,12]

Regarding torque control of the HWT, Dutta[13] proposed the application of a proportional-integral (PI) controller to regulate the torque by controlling the displacement of the motor to track the command of pressure differences across the pump, which is computed from the pump torque command (denoted as $K\omega^2$ law). However, the PI controller does not provide good tracking performance under turbulent wind. Rapp[14] applied a PI/PID controller, which directly optimises the tip-speed ratio (denoted as *DTSRT* law) with a feed-forward scheme. The results from this indicate that the performance of *DTSRT* law is slightly worse than the $K\omega^2$ law, and the feed-forward scheme does not provide a distinct advantage under real wind conditions. Wang et al[15] proposed applying the model predictive control (MPC) to track the optimal tip-speed ratio; however, this only provides good tracking performance in a limited range of wind speeds. This is because the control design is based on a linearised model, which does not take into account all the uncertainties or interactions with other dynamics in realistic scenarios, such as wave conditions, tower vibrations, and blade flap oscillations. Furthermore, for the HWT, the equilibrium selection for system linearisation is highly dependent on the wind speed, which inherently introduces modelling error in the linearised system since wind speed always varies in practice. That is, the control performance would inevitably be influenced because of the inaccuracy of the system modelling. Tong and Zhao[16] employed an $\mathcal{H}_\infty$ loop-shaping controller to regulate the motor displacement, which shows good performance, but such a control design also requires the system linearisation, and the high-order $\mathcal{H}_\infty$ controller often leads to difficult commissioning in practice.

In terms of pitch control for the HWT, PI controllers are normally utilised, which includes a standard PI controller with antiwindup,[13] gain-scheduling integral controller (*I*-controller),[17] gain-scheduling PI controller,[18] and gain-scheduling PI controller with antiwindup.[16,19] However, the disturbance rejection performance of these controllers under turbulent winds are limited, and the transition between region 2 and 3 is not smooth enough. Tong and Zhao[16] proposed a linear-parameter-varying (LPV) pitch controller based on LIDAR wind preview and compared it with the gain-scheduling PI controller designed by Laguna.[18] Their results showed that the LPV controller provides much better performance than the gain-scheduling PI controller in both disturbance rejection and tower vibration reduction.[16] However, as the LPV controller was designed based on the single-DOF linearised models without considering the interaction with other dynamics such as tower vibration or blade flap oscillations, this may degrade the control performance in practical scenarios.

In the present paper, we will employ the model-free adaptive control (MFAC) method to realise torque control and pitch control for the HWT, in order to overcome the disadvantages of the above controllers mentioned above and improve control performance. The MFAC is a novel dynamic linearisation method based on real-time system input and output measurement data that eliminates the need for establishing a mathematical model of the system plant, which improves the robustness with regard to modelling errors caused by the selection of operation points. Additionally, it is an easily applicable control scheme, with low computational burden and strong robustness.[20] The application of MFAC controller in power control systems has already been investigated previously, such as the applications of the power control system stabilizer,[21] AC/DC microgrid,[22] and wind turbine load control.[23] In this paper, we specifically investigate the MFAC control's application on power generation control in the HWT. The simulation results obtained indicate that the MFAC algorithm provides outstanding tracking effectiveness and disturbance rejection performance with reduced fatigue load on the wind turbine tower as compared with other controllers.

This paper is structured as follows: In Section 2, we briefly introduce the HWT structure with its mathematical models. In Section 3, we expatiate the MFAC algorithm and the design of $\mathcal{H}_\infty$ torque controller and gain-scheduling PI pitch controller. In Section 4, we conduct simulations and compare the performance of the MFAC controller and $\mathcal{H}_\infty$ and gain-scheduling PI controllers. Finally, Section 5 concludes this paper.

2 | INTRODUCTION ON A HYDROSTATIC TRANSMISSION DRIVETRAIN

This paper employs the detailed HWT simulation model developed by Tong and Zhao,[16] which is transformed from the NREL 5-MW gearbox-based wind turbine model within FAST (fatigue, aerodynamics, structures, and turbulence) code[12,24,25] by replacing its gearbox drivetrain with a HST. Because of this, we think this HWT simulation model has big potential to be widely applicable for HWT research. In this section, we briefly introduce its HST model. As shown in Figure 1, the HST is composed of a pump and a motor. The pump converts the mechanical energy into the pressurised oil, which drives the motor to generate electrical power. Either of the pump or the motor can be variable. In this paper, we use a variable displacement pump. We mention that the pipeline dynamics here is described by a linear model, which does not take the nonlinear characteristics into considerations, such as fluid compressibility in enclosed space. But this does not affect power generation control research.

Equations (1) to (5) show the mathematical model of the variable displacement pump and fixed displacement motor; Equations (6) to (7) elaborate the dynamics of the fluid transmission line with assumption of constant pressure in low pressure line.[16,18] The matrices $A_l, B_{l1}, B_{l2}, C_{l2}, C_{l2}$ are defined in terms of the physical parameters of the hydraulic line, such as the pipe inner radius, fluid density, and kinematic viscosity. This fluid transmission line model has been explained in details in many literatures.[18,26,27] In this paper, the pipeline model has 21 states, and we use a 10-m

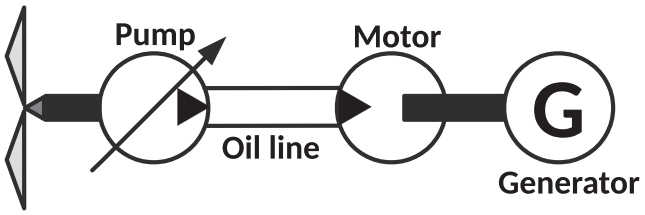

FIGURE 1 Hydrostatic transmission (HST) drivetrain configuration in a hydrostatic wind turbine (HWT) with their connections

transmission line with internal radius of 0.125 m, fluid density of 917 kg/m^3, kinematic viscosity of 40×10^{-6} m^2/s, and effective bulk modulus of 10^9 Pa.

$$Q_p = D_p\omega_r - C_{sp}p_p, \tag{1}$$

$$\tau_p = (1 + C_{fp})D_p p_p + B_p\omega_r, \tag{2}$$

$$\dot{D}_p = \frac{1}{T_p} \cdot (D_p^* - D_p), \tag{3}$$

$$Q_m = D_m\omega_m + C_{sm}p_m, \tag{4}$$

$$\tau_m = (1 + C_{fm})D_m p_m - B_m\omega_m, \tag{5}$$

$$\dot{\mathbf{x}}_\mathbf{l} = \mathbf{A}_\mathbf{l}\mathbf{x}_\mathbf{l} + \begin{bmatrix}\mathbf{B}_{\mathbf{l}1} & \mathbf{B}_{\mathbf{l}2}\end{bmatrix} \begin{bmatrix} \mathrm{Q_p} \\ \mathrm{Q_m} \end{bmatrix}, \tag{6}$$

$$\begin{bmatrix} \mathrm{p_p} \\ \mathrm{p_m} \end{bmatrix} = \begin{bmatrix} \mathbf{C}_{\mathbf{l}1} \\ \mathbf{C}_{\mathbf{l}2} \end{bmatrix} \mathbf{x}_\mathbf{l}, \tag{7}$$

where Q, τ, D, C_s, p, C_f, and B represent the volumetric flow rate, transmitted torque, volumetric displacement, laminar leakage coefficient, the pressure difference, the Coulomb friction coefficient and the viscous damping coefficient, respectively, with the subscripts "p" and "m" representing the pump and motor.[16,18,28] D_p^* represents the command of the pump volumetric displacement, and T_p represents the time constant. ω_r represents the wind turbine rotor speed. ω_m is the fixed rotational speed of motor and generator.

The rotational dynamics of the wind turbine rotor shaft is modelled as follows:

$$\dot{\omega}_r = \frac{1}{J_r + J_p} \cdot [\tau_{aero}(\omega_r, \beta, v_{wind}) - \tau_p], \tag{8}$$

where J_r and J_p are the rotational inertia of the wind turbine rotor and pump. τ_{aero} is the aerodynamic torque applied to the wind turbine rotor. The pitch actuator is modelled as

$$\dot{\beta} = \frac{1}{T_\beta} \cdot (\beta^* - \beta), \tag{9}$$

where β^* and β represent the command and actual blade pitch angles in degree respectively, and T_β represents the time constant. The power captured by wind turbine is

$$P = \frac{1}{2}\rho_{air}\pi R^2 v_{wind}^3 C_p(\lambda, \beta), \tag{10}$$

where ρ_{air} is the air density, R is the blade length, and v_{wind} is the wind speed.[11] C_p is the power coefficient, which is a function of tip-speed-ratio λ ($\lambda = \frac{\omega_r R}{v_{wind}}$) and pitch angle β. [11] Therefore, according to Equations (8) and (10), through properly control of the pump torque τ_p and pitch angle β, we are able to capture the desired amount of power from wind.

3 | CONTROL ALGORITHMS

In this section, we will explain the control algorithms applied in this paper. The model-free adaptive control (MFAC) was originally proposed by Hou et al[20] and slightly improved here. We will expatiate the general theory of the model-free adaptive control (MFAC) scheme for a discrete-time single-input-single-output (SISO) nonlinear system[20,29-31] and explain its control design procedure and control algorithm for both pump torque control and pitch control in the HWT system. Additionally, we will also design a $\mathcal{H}_\infty$ torque controller and explain gain-scheduling PI pitch controller.

3.1 | MFAC preliminary

The discrete-time SISO nonlinear system is written as

$$y(k+1) = f(y(k), \ldots, y(k - n_y), u(k), \ldots, u(k - n_u)), \tag{11}$$

where $y(\cdot)$ is the system output signal, and $u(\cdot)$ is the system input signal, $f(\cdots)$ represents the nonlinear system plant, n_y and n_u are two unknown positive integers. If system (11) satisfies the following two assumptions, the partial form dynamic linearisation (PFDL) data model can be derived as in Theorem 1.

Assumption 1. The partial derivatives of $f(\cdots)$ with respect to the variables $u(k), \ldots, u(k-L+1)$ are continuous, where L is called the linearisation length constant (LLC) of the discrete-time nonlinear system.[31]

Assumption 2. The system (11) satisfies the generalised Lipschitz condition, that is, $|\Delta y(k+1)| \le b \|\Delta \boldsymbol{U}_L(k)\|$, in which b is a positive constant, $\Delta \boldsymbol{U}_L(k) = \boldsymbol{U}_L(k) - \boldsymbol{U}_L(k-1)$, $\Delta y(k) = y(k) - y(k-1)$, and $\boldsymbol{U}_L(k) = [u(k), \ldots, u(k-L+1)]^T$.[31]

Here, *Assumption* 1 explicates the conventional condition of control design for the nonlinear system, and *Assumption* 2 introduces an upper bound for the system output changing rate.[31]

Theorem 1. *For the nonlinear system (11), which satisfies the Assumption 1 and Assumption 2, there must exist a time-varying parameter vector $\boldsymbol{\phi}_L(k)$, with $\boldsymbol{U}_L(k) \neq 0$ for all k, such that the system (11) can be written as the following equivalent PFDL description:*[31]

$$\Delta y(k+1) = \boldsymbol{\phi}_L^T(k) \Delta \boldsymbol{U}_L(k), \tag{12}$$

where the vector $\boldsymbol{\phi}_L(k) = [\phi_1(k), \ldots, \phi_L(k)]^T$ is bounded at any time k. The proof of this theorem can be found in Hou et al.[20,31]

The parameter vector $\boldsymbol{\phi}_L(k)$ in Theorem 1 is called the pseudo gradient (PG) vector. From Theorem 1, it is clear that through estimating this time-varying PG vector, we are able to establish an equivalent linearised model (PFDL model) for the SISO nonlinear system (11).

The index functions for PG estimation are defined as

$$J(\hat{\boldsymbol{\phi}}_L(k)) = \left| y(k) - y(k-1) - \hat{\boldsymbol{\phi}}_L^T(k) \Delta \boldsymbol{U}_L(k-1) \right|^2 + \mu \left\| \hat{\boldsymbol{\phi}}_L(k) - \hat{\boldsymbol{\phi}}_L(k-1) \right\|^2 \tag{13}$$

in which $\mu > 0$ is a weighting factor. $\hat{\boldsymbol{\phi}}_L(k)$ denotes the estimation of PG vector $\boldsymbol{\phi}_L(k)$ at time k.

The index functions for control input is defined as

$$J(u(k)) = |y^*(k+1) - y(k+1)|^2 + \alpha |u(k) - u(k-1)|^2, \tag{14}$$

where $y^*(\cdot)$ is the desired reference signal. $\alpha > 0$ is the weighting constant.

By optimising these two index functions, the MFAC algorithm for SISO systems are given as

$$\hat{\boldsymbol{\phi}}_L(k) = \hat{\boldsymbol{\phi}}_L(k-1) + \eta \Delta \boldsymbol{U}_L(k-1) \cdot \frac{y(k) - y(k-1) - \hat{\boldsymbol{\phi}}_L^T(k-1) \Delta \boldsymbol{U}_L(k-1)}{\mu + \|\Delta \boldsymbol{U}_L(k-1)\|^2}, \tag{15}$$

$$\hat{\boldsymbol{\phi}}_L(k) = \hat{\boldsymbol{\phi}}_L(1), \text{if} \begin{cases} \left\| \hat{\boldsymbol{\phi}}_L(k) \right\| \le \epsilon, & \text{or} \\ \text{sign}(\hat{\phi}_1(k)) \neq \text{sign}(\hat{\phi}_1(1)), & \text{or} \\ \|\Delta \boldsymbol{U}_L(k-1)\| \le \epsilon, \end{cases} \tag{16}$$

and

$$u(k) = u(k-1) + \frac{\rho_1 \hat{\phi}_1(k)(y^*(k+1) - y(k))}{\alpha + \left| \hat{\phi}_1(k) \right|^2} - \frac{\hat{\phi}_1(k) \sum_{i=2}^{L} \rho_i \hat{\phi}_i(k) \Delta u(k-i+1)}{\alpha + \left| \hat{\phi}_1(k) \right|^2}, \tag{17}$$

where $\mu > 0$, $\alpha > 0$, step-size constant $\eta \in (0, 2)$, and step-size vector $\rho_i \in (0, 1]$. ϵ is a small positive constant, and $\hat{\boldsymbol{\phi}}_L(1)$ is the initial of $\hat{\boldsymbol{\phi}}_L(k)$. The reset mechanism (16) is added for a strong tracking capability for the time-varying PG vector. From (15) to (17), it is clear that the control law $u(k)$ only depends on the system input and output measurements, which implies the model free nature of the approach.

Considering the stability analysis of the MFAC scheme, we have Theorem 2, which is deducted based on *Assumption* 3. Detail of the proof can be found in Hou et al.[31]

Assumption 3. The sign of the first element in PG vector $\boldsymbol{\phi}_L(k)$ is assumed to be unchanged for all k with $\|\Delta \boldsymbol{U}_L(k)\| \neq 0$. That is, $\phi_1(k) > \epsilon > 0$ (or $\phi_1(k) < -\epsilon < 0$), where ϵ is a small positive constant.[31]

Theorem 2. *If the nonlinear system (11) satisfies the Assumption 1, 2, 3 and is controlled by the MFAC algorithms (15) to (17), there exists a constant $\alpha_{min} > 0$, such that for any $\alpha > \alpha_{min}$, the system output tracking error converges to zero asymptotically, and system $y(k)$ and $u(k)$ are bounded for all k, which indicates the closed-loop system is bounded-input-bounded-output (BIBO) stable.*[31]

Based on the MFAC scheme (15) to (17), the characteristics of the HWT system including the effect of tower vibration, blade flap oscillations, and turbulent wind are all integrated into the estimated pseudo gradient (PG). Since Theorem 2 indicates a monotonic change between system output and control input, extra damping terms are required for adjustment of the closed-loop system dynamics to meet the performance specifications in the desired control bandwidth of the HWT power generation system. Additionally, the step-size vector $\boldsymbol{\rho}$ serves as the proportional gain of

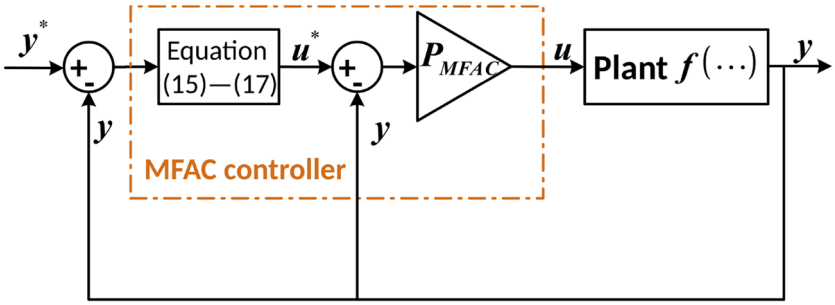

FIGURE 2 Block diagram MFAC control scheme. Note that in the following of this paper, "MFAC controller" is referred to the control scheme with damping term P_{MFAC} displayed in this figure [Colour figure can be viewed at wileyonlinelibrary.com]

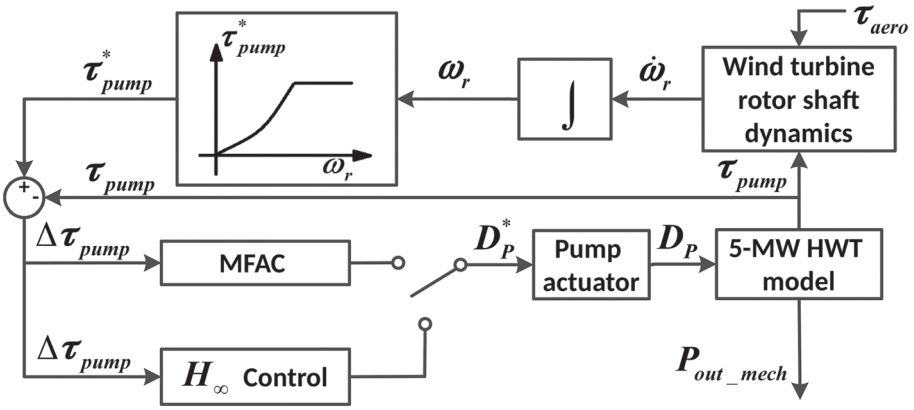

FIGURE 3 Block diagram of torque control scheme

the closed-loop system (see (17)), where larger step-size vector contributes to the faster dynamic response. However, without damping effect, increasing proportional gain may lead to the undesirable overshoot, oscillations, or even unstable dynamics. Hence, to have a good dynamic response in the desired control bandwidth, it is of great significance to have the extra damping term. We improve the MFAC control scheme by introducing the extra damping term P_{MFAC} (see Figure 2). The damping term P_{MFAC} is used to serve as the damping gain suppressing the oscillations in the system output y. The newly established MFAC controller (see Figure 2) is able to provide good dynamic performance without sacrificing the rising time. Note that the damping gain should be properly selected to ensure the system from u^* to y satisfies *Assumption* 1 and *Assumption* 2. In the following context, the "MFAC controller" is referred to the improved control scheme with damping term P_{MFAC} as shown in Figure 2.

3.2 | Torque control design

The objective of the torque controller is to minimise the tracking error between the pump torque command τ_p^* and pump torque τ_p via regulating the pump volumetric displacement command D_p^*. The pump torque command τ_p^* is obtained from the $K\omega_r^2$ law provided by Jonkman et al.[12] See Figure 3 for the block diagram of the torque control scheme. Firstly, we design a $\mathcal{H}_\infty$ loop-shaping torque controller based on the HWT model explained in Section 2. Then we design a MFAC torque controller, making comparison to the performance of $\mathcal{H}_\infty$ loop-shaping torque controller under different wind speeds. The control parameters of this MFAC torque controller are listed as follows: $\alpha = 6.6 \times 10^{13}$, $\rho_1 = \rho_2 = \rho_3 = 0.8424$, $\Phi_L(1) = [10^7\, 10^7\, 10^7]^T$, $\eta = 1$, $\mu = 1$, $P_{MFAC} = 15$.

Here, we briefly describe the design procedure of $\mathcal{H}_\infty$ loop-shaping torque controller. It is designed based on the systems (1) to (8) linearised at the operating point ($\bar{\omega}_r = 10.3$ rpm, $\bar{v}_{wind} = 9$ m/s and $\bar{\beta} = 0°$):

$$\dot{\hat{\mathbf{x}}}_{\tau c} = A_{\tau c}\hat{\mathbf{x}}_{\tau c} + B_{\tau c}\hat{D}_p^* + \mathbf{B}_{\tau cd}\hat{\mathbf{d}}, \tag{18}$$

$$\hat{\tau}_p = \mathbf{C}_{\tau c}\hat{\mathbf{x}}_{\tau c} + D_{\tau c}\hat{D}_p^*, \tag{19}$$

in which $\hat{\mathbf{x}}_{\tau c} = \mathbf{x}_{\tau c} - \bar{\mathbf{x}}_{\tau c} = \left[\hat{\omega}_r \quad \hat{D}_p \quad \hat{\mathbf{x}}_{\mathrm{I}}\right]^T$, $\hat{D}_p^* = Dp^* - \bar{D}_p$, $\hat{d} = d - \bar{d} = \hat{v}_{wind}$, and $\hat{\tau}_p = \tau_p - \bar{\tau}_p$.

The matrices $\mathbf{A}_{\tau c}$, $\mathbf{B}_{\tau c}$, $\mathbf{C}_{\tau c}$, $D_{\tau c}$ are derived as

$$\mathbf{A}_{\tau c} = \begin{bmatrix} \frac{\frac{\partial \tau_{aero}}{\partial \omega_r} - B_p}{J_r + J_p} & \frac{-(1+C_{fp})\mathbf{C}_{\mathrm{I}1}\bar{\mathbf{x}}_{\mathrm{I}}}{J_r + J_p} & \frac{-(1+C_{fp})\mathbf{C}_{\mathrm{I}1}\bar{D}_p}{J_r + Jp} \\ 0 & -\frac{1}{T_p} & \mathbf{0} \\ \mathbf{B}_{\mathrm{I}1}\bar{D}_p & \mathbf{B}_{\mathrm{I}1}\bar{\omega}_r & \mathbf{A}_{\mathrm{I}} - C_{sp}\mathbf{B}_{\mathrm{I}1}\mathbf{C}_{\mathrm{I}1} + C_{sm}\mathbf{B}_{\mathrm{I}2}\mathbf{C}_{\mathrm{I}2} \end{bmatrix}; \tag{20}$$

$$\boldsymbol{B}_{\boldsymbol{\tau c}} = \left[0 \ \frac{1}{T_p} \ \boldsymbol{0}\right]^T; \tag{21}$$

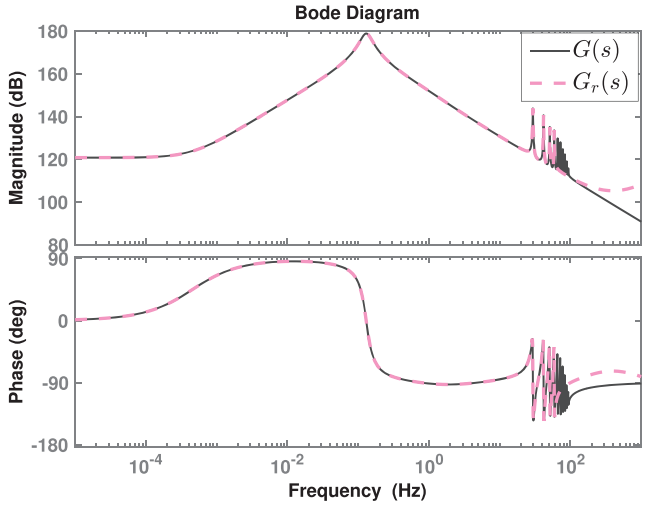

FIGURE 4 Bode diagram of the system $G(s)$ and the reduced-order system $G_r(s)$ [Colour figure can be viewed at wileyonlinelibrary.com]

$$\mathbf{B}_{\tau cd} = \begin{bmatrix} \frac{\frac{\partial \tau_{aero}}{\partial v_{wind}}}{J_r + J_p} \\ 0 \\ \mathbf{0} \end{bmatrix}; \tag{22}$$

$$\mathbf{C}_{\tau c} = \begin{bmatrix} B_p & (1 + C_{fp})\mathbf{C}_{\mathbf{l}1}\tilde{\mathbf{x}}_{\mathbf{l}} & (1 + C_{fp})\mathbf{C}_{\mathbf{l}1}\bar{D}_p \end{bmatrix}; \tag{23}$$

$$D_{\tau c} = [0]. \tag{24}$$

The system from pump displacement command D_p^* to pump torque τ_p are denoted as $G(s)$ with its state-space realisation $(\mathbf{A}_{\tau c}, \mathbf{B}_{\tau c}, \mathbf{C}_{\tau c}, D_{\tau c})$. $G(s)$ is a 23-order system. We reduce the system order by discarding 11 states with relatively small Hankel singular values through matching DC-gain method, which is implemented by Matlab command "*balred*."[32-35] It computes the reduced-order approximation of a LTI model while preserving the dynamics of the original system in the interested range for control design purpose. From Figure 4, it is clear that the reduced-order system $G_r(s)$ matches the original system $G(s)$ well in the low frequency range ($\lesssim$ 63 Hz). Then the $\mathcal{H}_\infty$ controller is designed based on this reduced system by using Matlab command "*loopsyn*,"[36-41] which computes the stabilising controller that best approximates the prespecified desired open-loop shape. The selected desired loop shape is

$$G_d = \frac{30000}{(s + 10^{-5})(s + 1000)}. \tag{25}$$

3.3 | Pitch control design

The purpose of the pitch controller is to stabilise the wind turbine rotor speed ω_r at its rating in region 3. This is implemented through regulating the blade pitch angle command β^*. Note that the pitch angle is forced to 0° in region 2. See Figure 5 for the block diagram of pitch control scheme. We design the pitch controller by using the MFAC scheme in Figure 2. The parameters of MFAC pitch controller are listed as follows: $\alpha = 5$, $\rho_1 = \rho_2 = \rho_3 = 7.8 \times 10^{-4}$, $\Phi_L(1) = [131313]^T$, $\eta = 1$, $\mu = 1$, $P_{MFAC} = -40$.

The performance of MFAC pitch controller is then compared with that of the gain-scheduling PI controller designed by LagunaHWT1 and of the gain scheduling PI controller with antiwindup (PIAW) designed by Tong and Zhao.[16] The antiwindup compensation for the gain-scheduling PI controller is designed to mitigate the undesirable system response owing to pitch saturation and to cancel out the undesirable negative angles brought by the integrator.[16] The selection of the gain-scheduling PI parameters (K_{pgs} and K_{igs}) and antiwindup parameter (K_{aw}) follows that of Laguna[18] and Tong and Zhao[16]:

$$K_{pgs} = -\frac{1.6167}{1 + \frac{\beta}{6.302336}}, \tag{26}$$

$$K_{igs} = -\frac{0.6929}{1 + \frac{\beta}{6.302336}}, \tag{27}$$

$$K_{aw} = 0.5. \tag{28}$$

4 | SIMULATION STUDIES

In this paper, we test the performance of the MFAC torque and pitch controller on a 5-MW HWT, whose dynamic responses are simulated in Matlab/Simulink environment using the modified NREL FAST code. The parameters for the HWT system are listed in Table 1.

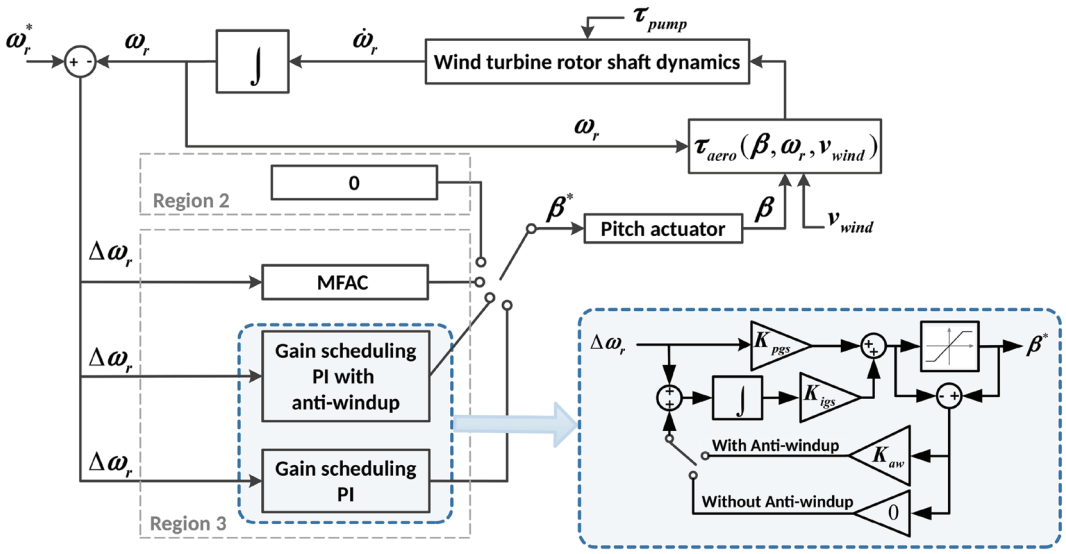

FIGURE 5 Block diagram of pitch control scheme, including the control block diagrams of gain-scheduling PI controller and gain-scheduling PI controller with antiwindup (PIAW) [Colour figure can be viewed at wileyonlinelibrary.com]

TABLE 1 Parameters for HWT system[18]

Symbol	Value	Unit	Symbol	Value	Unit
C_{sp}	7.1×10^{-11}	$m^3/(s{\cdot}Pa)$	C_{fp}	0.02	-
C_{sm}	7.0×10^{-11}	$m^3/(s{\cdot}Pa)$	C_{fm}	0.02	-
D_m	4.1609×10^{-4}	m^3/rad	B_p	50000	Nms
J_r	38759236	kgm^2	B_m	2.5	Nms
J_p	3680	kgm^2	T_p	0.1	s
ω_m	60	Hz	T_β	0.5	s
ρ_{air}	1.225	kg/m^3	R	61.5	m

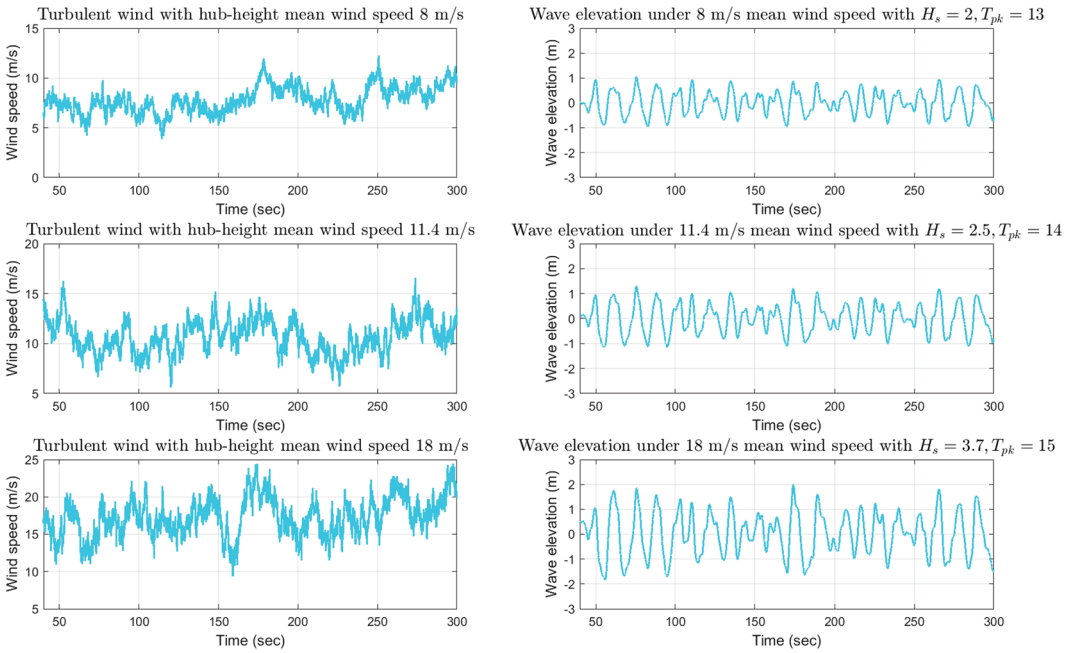

FIGURE 6 Turbulent wind with hub-height mean wind speeds of 8 m/s, 11.4 m/s, and 18 m/s and the wave elevations under the these three wind conditions. H_s (m) denotes the significant wave height of incident wave. T_{pk} (second) is the peak-spectral period of incident wave [Colour figure can be viewed at wileyonlinelibrary.com]

The simulations are conducted for 300 seconds at the hub height of 84 m under turbulent wind with mean wind speeds of 8, 11.4 (rated speed), and 18 m/s respectively. The International Electro-technical Commission (IEC) Kaimal spectral NTM (normal turbulence model)[42,43] in NREL Turbsim[44] was utilised to generate stochastic, full-field, and turbulent wind flows from which wind flows under category A (most turbulent) have been selected for this study. The turbulence intensity in percentage and the standard deviation of the longitudinal wind speed at hub-height

under category A is related to the mean wind speed at hub-height. For mean wind speeds of 8, 11.4, and 18 m/s, the turbulence intensities are roughly 23.5%, 19.5%, and 17% respectively, and the standard deviations of the longitudinal wind speed at hub-height are roughly 1.88, 2.22, and 3.06 m/s, respectively.[44] The time step to generate the turbulent wind series is 0.05 seconds. See Figure 6 for the turbulent wind speeds and the corresponding wave elevations. The wave conditions are generated by using the JONSWAP irregular wave spectrum.[45] The significant wave height (and the peak-spectral period) of the incident wave under hub-height mean wind speeds of 8, 11.4, and 18 m/s are set to be 2 m (13 seconds), 2.5 m (14 seconds), and 3.7 m (15 seconds), respectively.[45]

4.1 | Torque control performances

In region 2, the pump torque command τ_p^* is proportional to the square of the wind turbine rotor speed ω_r, which instructs the wind turbine to maintain the optimal tip-speed ratio and realising MPPT operation.[12] This means that based on accurate regulation of pump torque, the optimal tip-speed ratio can be achieved, and the accuracy of the regulation will directly influence the amount of power captured from the wind. When wind turbine operates in region 3, the power extraction depends on both the pitch and torque controllers. The performance of the MFAC torque controller and the $\mathcal{H}_\infty$ torque controller are compared through the root-mean-square (RMS) value of the tracking error:

$$\text{RMS}_\tau = \sqrt{\frac{1}{T_{sim}}\int_0^{T_{sim}} (\tau_p^* - \tau_p)^2 dt}, \tag{29}$$

where T_{sim} is 300 seconds.

We run the torque control simulations under the wind and wave conditions shown in Figure 6. The tracking performances of both the MFAC controller and the $\mathcal{H}_\infty$ controller under three different wind and wave conditions have been listed in Figures 8 to 10, respectively. The detailed performance comparison has been listed in Table 2, which shows the RMS_τ and power delivered to the generator under the control of the MFAC controller and the H_∞ controller, respectively, in three wind and wave conditions. Note that the power is the average mechanical power over the simulation period:

$$\text{Power} = \frac{1}{T_{sim}}\int_0^{T_{sim}} \tau_m \cdot \omega_m dt, \tag{30}$$

where T_{sim} is 300 seconds. Note that in Table 2, power extraction comparison is not provided when the mean wind speed is 18 m/s, as under this speed, the wind turbine operates in region 3, where power extraction is very relevant to pitch control.

Figure 7 shows the command of pump displacement under different wind and wave condtions. From Figures 8 to 10, it is clear that the MFAC controller shows better tracking performance with smaller oscillations than the $\mathcal{H}_\infty$ controller. Moreover, the performance of the MFAC controller shows no conspicuous differences under different wind speeds, while there is visible degradation in the performance of the $\mathcal{H}_\infty$ controller as the mean wind speed rises. This is due to the design of the $\mathcal{H}_\infty$ loop-shaping controller being based on the model linearised at wind

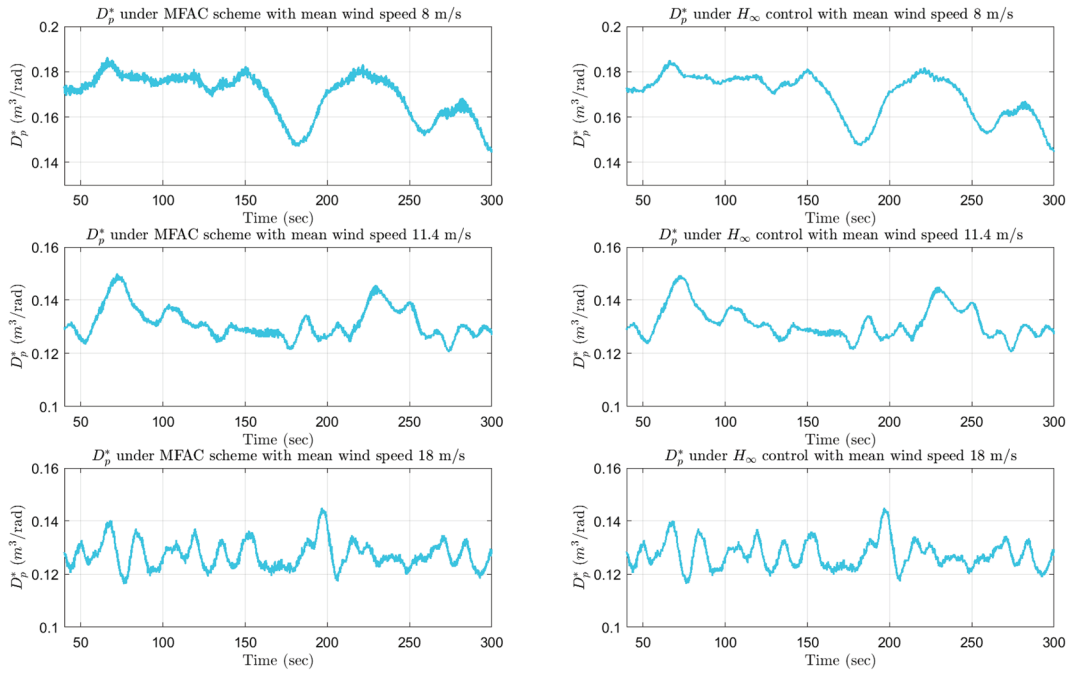

FIGURE 7 Command of pump displacement D_p^* under different wind and wave conditions [Colour figure can be viewed at wileyonlinelibrary.com]

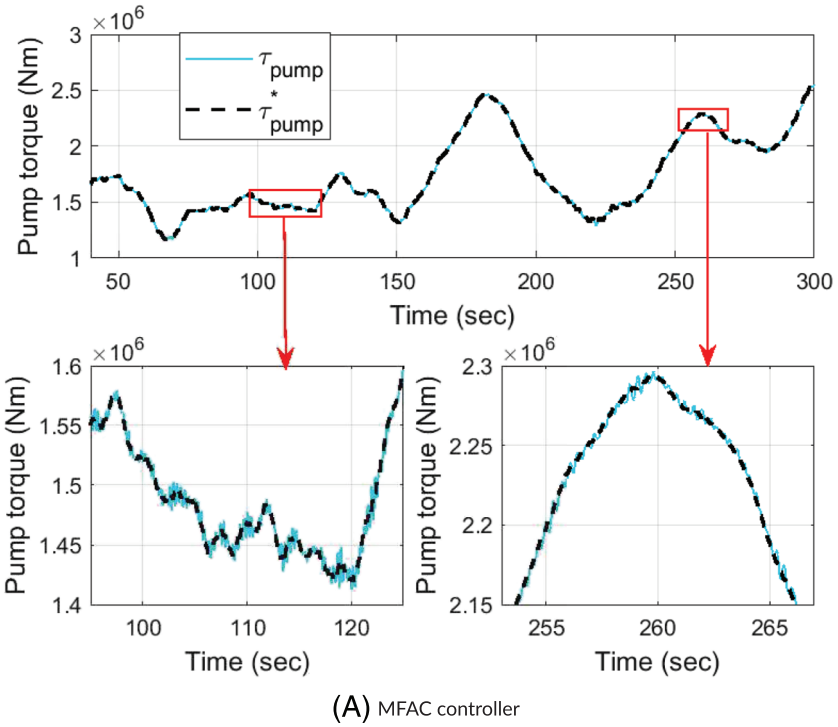

(A) MFAC controller

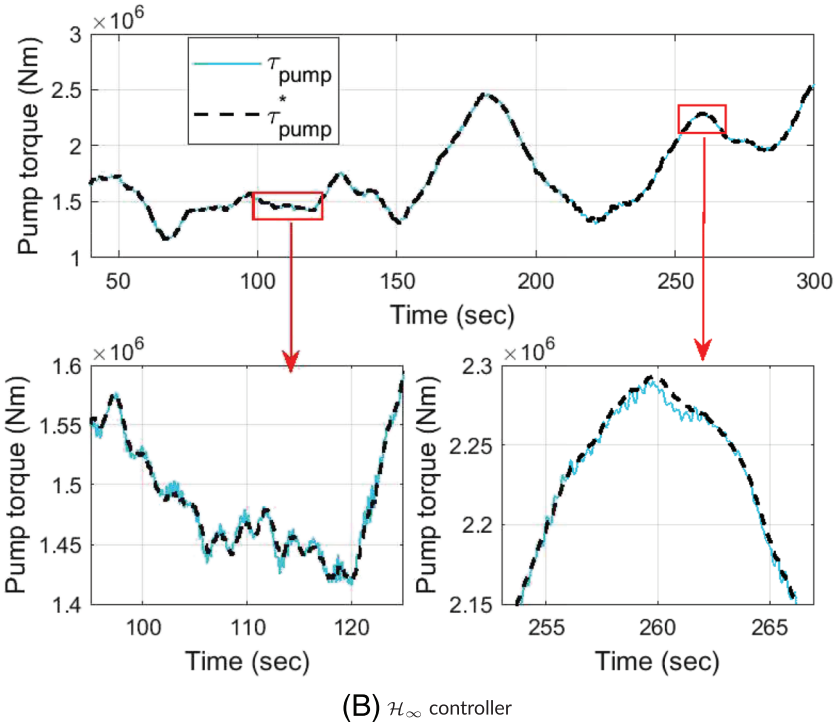

(B) $\mathcal{H}_\infty$ controller

FIGURE 8 Performances of pump torque control under turbulent wind with mean speed of 8 m/s [Colour figure can be viewed at wileyonlinelibrary.com]

speed of 9 m/s (see Section 3.2). Thus, as the mean wind speed moves away from 9 m/s, the $\mathcal{H}_\infty$ controller inevitably suffers from performance degradation because of modelling errors. However, the MFAC scheme is a model-free algorithm, which dynamically estimates the plant merely through exploiting the real-time input and output data. Thus, there are no obvious differences in the performances of the MFAC controller under different wind speeds. From Table 2, it is clear that the RMS_τ of the MFAC controller is much smaller than that of the $\mathcal{H}_\infty$ controller. Moreover, because of the high order of the $\mathcal{H}_\infty$ controller (16 orders here), it is not easily applicable in industries. These above points indicate that the MFAC controller potentially provides a better solution when compared with $\mathcal{H}_\infty$ controller.

4.2 | Pitch control performances

As the wind speed rises over 11.4 m/s (rated speed), the wind turbine rotor speed ω_r gradually increases to its rating ω_r^*. During this period, the wind turbine transits its operation region from region 2 to 3, and the pitch control is enabled to guarantee the steady power extraction, which

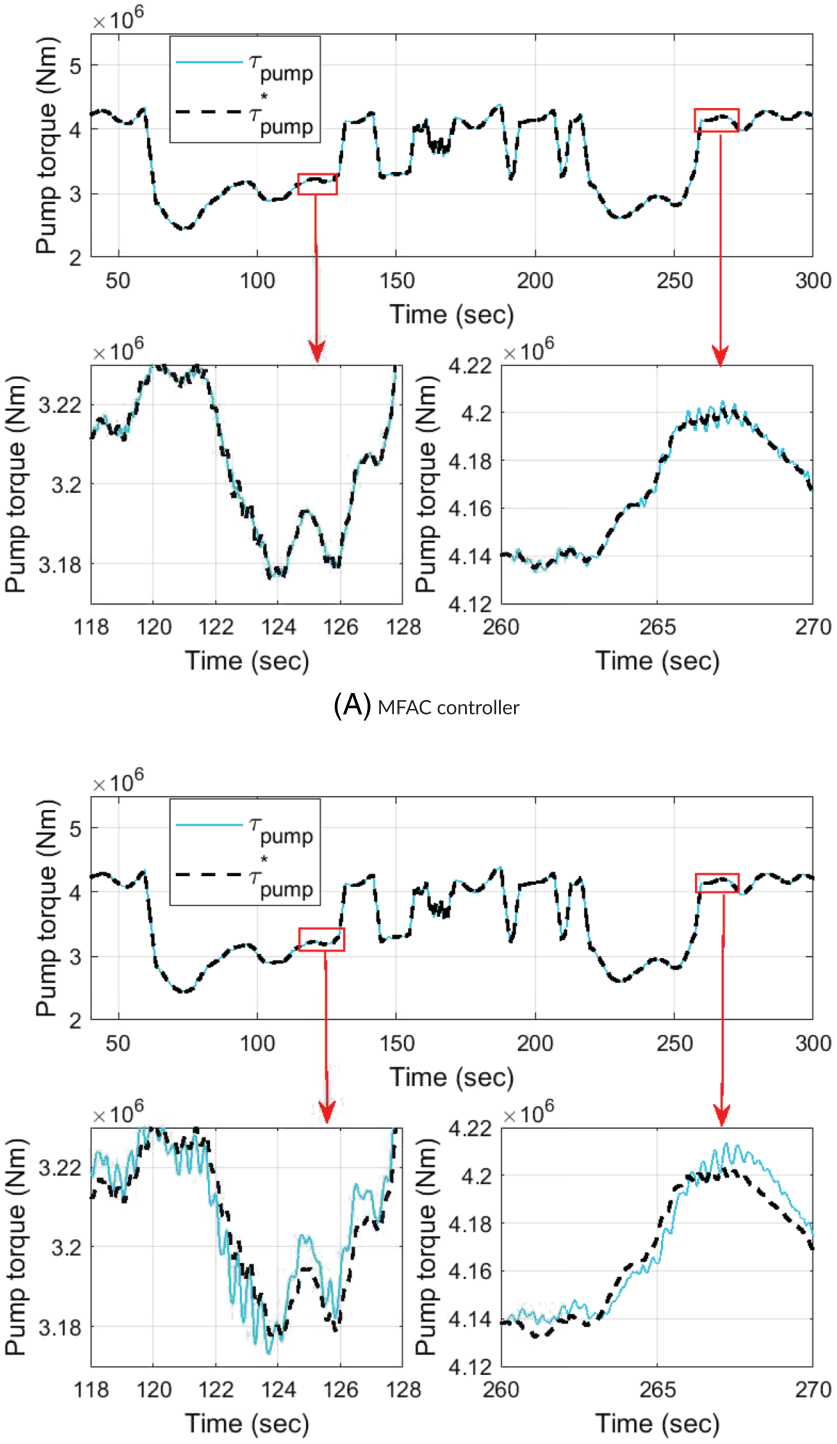

FIGURE 9 Performances of pump torque control under turbulent wind with mean speed of 11.4 m/s
[Colour figure can be viewed at wileyonlinelibrary.com]

ends the MPPT operation. A proper pitch control is expected to ensure smooth transitions with minimal overspeed in ω_r from region 2 to 3 as well as small variations in ω_r in region 3 regardless of turbulent wind speeds. We then calculate the root-mean-square value of the wind turbine rotor speed (RMS_{ω_r}) to evaluate the performance by different pitch control schemes:

$$\text{RMS}_{\omega_r} = \sqrt{\frac{1}{T_{sim}} \int_0^{T_{sim}} (\omega_r^* - \omega_r)^2 dt}, \tag{31}$$

where T_{sim} is 300 seconds. We calculate the mean power extraction for 300-second simulations and estimate the damage-equivalent load (DEL) under different pitch control schemes. The estimation procedure is implemented through the NREL MLife code based on the tower base side-side and fore-aft moment; this is a Matlab-based tool provided for fatigue life analysis.[46,47] The fatigue cycle is assumed to occur over a constant, or

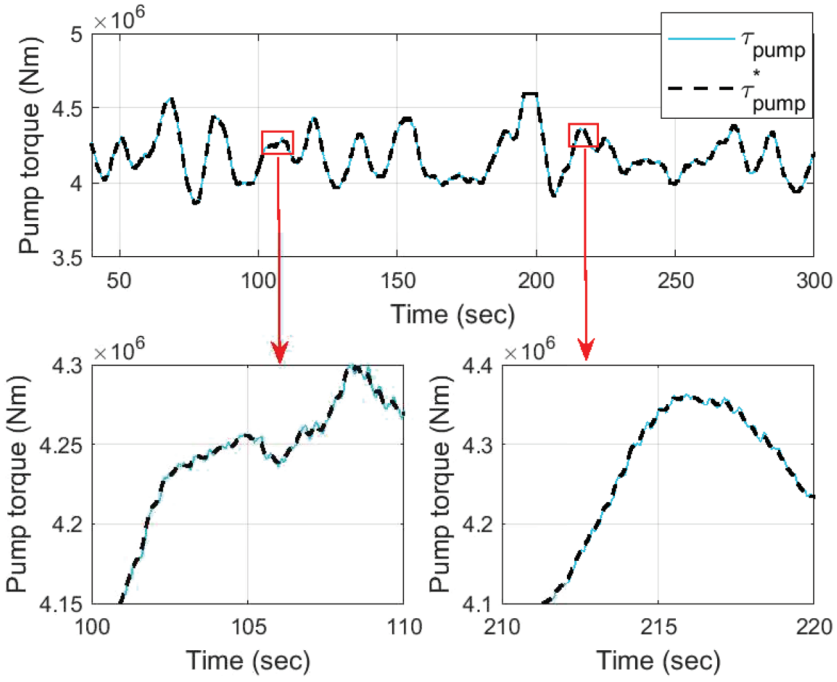

(A) MFAC controller

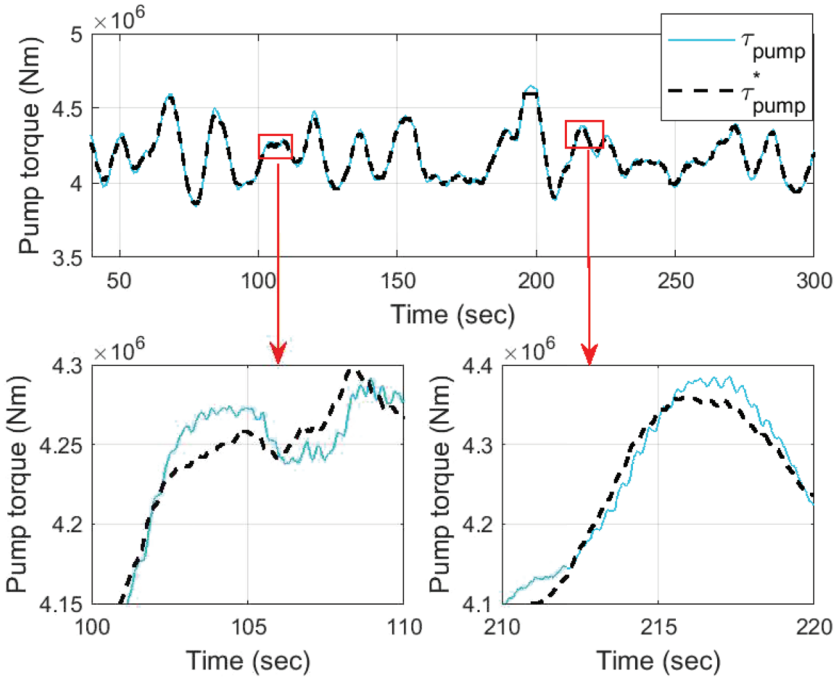

(B) $\mathcal{H}_\infty$ controller

FIGURE 10 Performances of pump torque control under turbulent wind with mean speed of 18 m/s [Colour figure can be viewed at wileyonlinelibrary.com]

	Wind	$\mathcal{H}_\infty$ Controller	MFAC Controller	Comparison (%)
RMS_τ (kN·m)	8 m/s	5.7806	5.7185	−1.07
	11.4 m/s	8.5823	4.0329	−53.01
	18 m/s	19.268	2.5443	−86.80
Power (MW)	8 m/s	1.2248	1.2258	+0.08
	11.4 m/s	3.8566	3.8871	+0.79
	18 m/s	4.7141	4.7141	–

Note. For average wind speed of 11.4 m/s and 18 m/s, the pitch controller is implemented by the gain-scheduling PI controller with anti-windup (PIAW). The comparison is calculated according to $\frac{\text{MFAC}-\mathcal{H}_\infty}{\mathcal{H}_\infty}$.

TABLE 2 Pump torque control performance implemented by the $\mathcal{H}_\infty$ controller and the MFAC controller

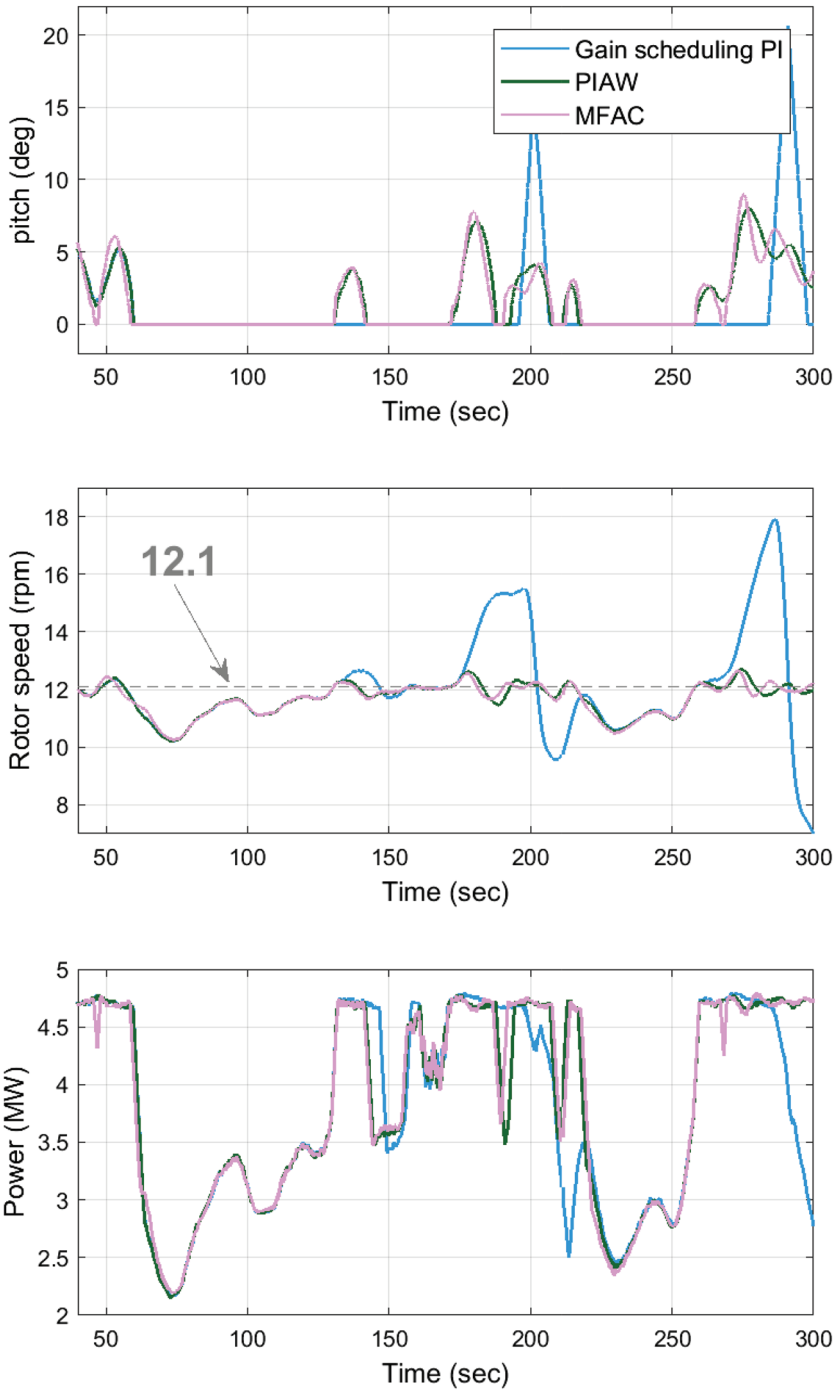

FIGURE 11 Pitch control performances (pitch angle, rotor speed, power extraction) by gain-scheduling PI controller, gain-scheduling PI controller with anti-windup (PIAW) and MFAC controller under mean wind speed of 11.4 m/s [Colour figure can be viewed at wileyonlinelibrary.com]

fixed load-mean, based on which the fatigue calculation will be conducted. In the fatigue load estimation, the ultimate load factor is selected to be 20, the number of range bins is selected to be 60, and the DEL frequency is set to be 1 Hz.

We run the simulations under mean wind speeds of 11.4 and 18 m/s (see Figure 6). The performances of the MFAC controller, gain-scheduling PI controller,[18] and gain-scheduling PI controller with antiwindup (PIAW)[16] under two wind speeds are displayed in Figures 11 and 12, respectively. The detailed performances and comparisons between three pitch control schemes are shown in Table 3. "Power" in Table 3 is the average mechanical power delivered to the generator over the simulation period, which is computed from Equation (30). The calculation of the RMS_{ω_r} under the mean wind speed of 11.4 m/s only considers the period when the wind turbine is in region 3 (when pitch angle $\beta \neq 0°$). Under mean wind speed of 18 m/s, the wind turbine operates only in region 3 with no pitch saturation, meaning that the antiwindup scheme is not enabled during this simulation. Hence, the performances of PIAW are not shown in Figure 12 since they are the same as the performances of the gain-scheduling PI controller.

The simulations show that every time the wind turbine transits from region 2 to 3, the MFAC controller provides the fastest rotor speed stabilisation performance without significant deviations from its reference. When the wind turbine remains in region 3, the power extraction by the MFAC controller is more steady, and the variation in rotor speed is much smaller in comparison with the gain-scheduling PI controller, which

	Wind (m/s)	Gain-scheduling PI	PIAW	MFAC controller	Comparison to gain-scheduling PI (%)	Comparison to PIAW (%)
RMS$_{\omega_r}$ (rpm)	11.4	2.5208	0.4665	0.4382	−82.62	−6.07
	18	0.4638	0.4638	0.2850	−38.55	−38.55
Power (MW)	11.4	3.7886	3.8566	3.8572	+1.81	+0.02
	18	4.7141	4.7141	4.7160	+0.04	+0.04
DEL	11.4	13.26	6.29	6.03	−54.52	−4.13
(MN·m)	18	9.27	9.27	8.63	−6.90	−6.90

TABLE 3 Wind turbine blade pitch control performance implemented by the gain-scheduling PI, PIAW and MFAC controller

Note. The pump torque control is implemented by $\mathcal{H}_\infty$ controller. The comparison to gain-scheduling PI and PIAW are calculated according to $\frac{\text{MFAC}-\text{PI}}{\text{PI}}$ and $\frac{\text{MFAC}-\text{PIAW}}{\text{PIAW}}$, respectively.

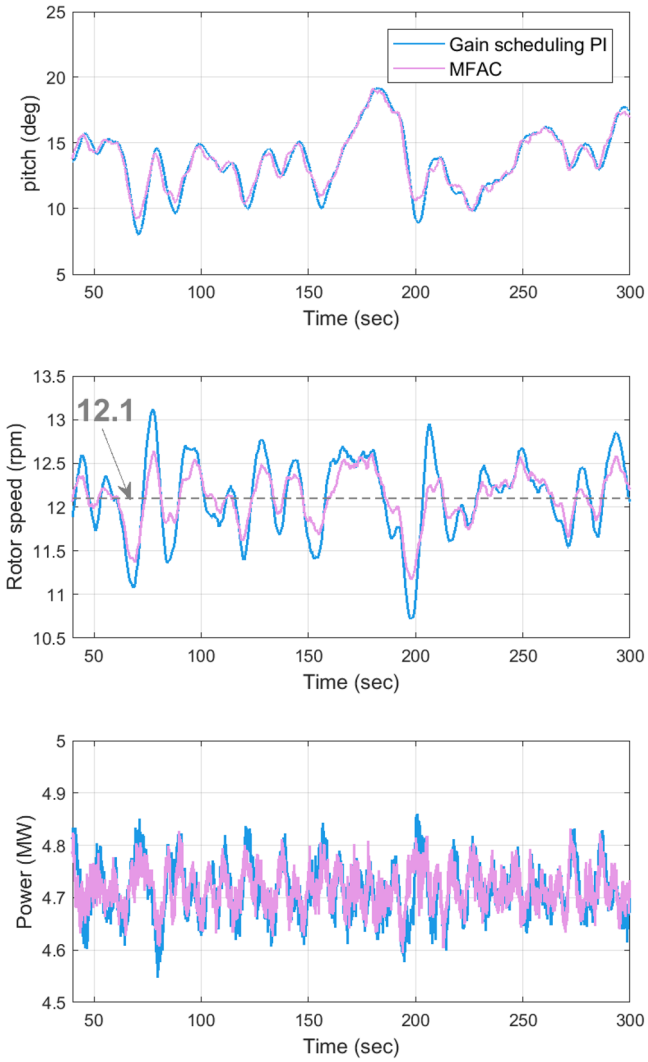

FIGURE 12 Pitch control performances (pitch angle, rotor speed, power extraction) by gain-scheduling PI controller and MFAC controller under mean wind speed of 18 m/s [Colour figure can be viewed at wileyonlinelibrary.com]

implies better disturbance rejection performance. Furthermore, less fatigue loads are exerted on the wind turbine tower base under the MFAC controller, which helps to extend the wind turbine fatigue life. Therefore, the MFAC is proven to have better performance to implement HWT pitch control than the gain-scheduling PI controller[18] and PIAW controller.[16] [Correction added on 21 January 2020, after first online publication: Figure 12 has been corrected]

5 | CONCLUSIONS

In this paper, the model-free adaptive control (MFAC) scheme was used for the power generation control (including both the torque and pitch control) of a 5-MW hydrostatic wind turbine (HWT). In simulations, the performances of a MFAC torque controller was compared with a $\mathcal{H}_\infty$ loop-shaping torque controller. The MFAC pitch controller was compared with a gain-scheduling PI controller[18] and a gain-scheduling PI controller with antiwindup.[16] The simulations results indicated that the MFAC torque controller provided superior performance over the $\mathcal{H}_\infty$ controller with faster responses and smaller oscillation and that the MFAC pitch controller had best rotor speed stabilisation capabilities and smoothest

transition between operation region 2 and 3 with least fatigue loads acting on the wind turbine tower. We have done many simulations besides the cases on this paper. All gets similar results. All these demonstrated that MFAC is a promising algorithm with high potential for the power generation control of the HWT. We mention that seriously inaccurate measurements may lead to disastrous control performance in practical situations, but it is also true for the traditional model-based control as they depend on the same feedback signal.

ORCID

Shuyue Lin https://orcid.org/0000-0002-2801-0257
Xiaowei Zhao https://orcid.org/0000-0002-1182-4502

REFERENCES

1. Twidell J, Weir T. *Renewable Energy Resources*. London, United Kingdom: Routledge; 2015.
2. Fornasiero P, Graziani M. *Renewable Resources and Renewable Energy: A Global Challenge*. Hoboken, NJ: CRC Press; 2011.
3. Ribrant J, Bertling L. Survey of failures in wind power systems with focus on swedish wind power plants during 1997-2005. In: IEEE Power Engineering Society General Meeting; 2007; Tampa, USA:1-8.
4. Silva P, Giuffrida A, Fergnani N, et al. Performance prediction of a multi-MW wind turbine adopting an advanced hydrostatic transmission. *Energy*. 2014;64:450-461.
5. Carroll J, McDonald A, McMillan D. Failure rate, repair time and unscheduled O & M cost analysis of offshore wind turbines. *Wind Energy*. 2016;19(6):1107-1119.
6. Tavner P, Xiang J, Spinato F. Reliability analysis for wind turbines. *Wind Energy Int J Prog Appl Wind Power Conver Technol*. 2007;10(1):1-18.
7. Faulstich S, Hahn B, Tavner PJ. Wind turbine downtime and its importance for offshore deployment. *Wind Energy*. 2011;14(3):327-337.
8. Huang H, Mao C, Lu J, Wang D. Small-signal modelling and analysis of wind turbine with direct drive permanent magnet synchronous generator connected to power grid. *IET Renew Power Gener*. 2012;6(1):48-58.
9. Polinder H, Van der Pijl FF, De Vilder GJ, Tavner PJ. Comparison of direct-drive and geared generator concepts for wind turbines. *IEEE Trans Energy Conver*. 2006;21(3):725-733.
10. Dreidy M, Mokhlis H, Mekhilef S. Inertia response and frequency control techniques for renewable energy sources: A review. *Ren Sustain Energy Rev*. 2017;69:144-155.
11. Johnson KE, Pao LY, Balas MJ, Fingersh LJ. Control of variable-speed wind turbines: standard and adaptive techniques for maximizing energy capture. *IEEE Control Syst*. 2006;26(3):70-81.
12. Jonkman J, Butterfield S, Musial W, Scott G. Definition of a 5-MW reference wind turbine for offshore system development. *Tech. Rep*. No. NREL/TP-500-38060, Golden, CO; 2009.
13. Dutta R. Modeling and analysis of short term energy storage for mid-size hydrostatic wind turbine. *Master thesis*: University of Minnesota; 2012.
14. Rapp J, Turesson J. Hydrostatic transmission in wind turbines: development of test platform. *Master thesis*: Linköping University; 2015.
15. Wang F, Stelson KA. Model predictive control for power optimization in a hydrostatic wind turbine. In: 13th Scandinavian International Conference on Fluid Power Linköping University Electronic Press; 2013; Linköping; Sweden:155-160.
16. Tong X, Zhao X. Power generation control of a monopile hydrostatic wind turbine using an H_∞ loop-shaping torque controller and an LPV pitch controller. *IEEE Trans Control Syst Technol*. 2018;26(6):2165–2172.
17. Skaare B, Hörnsten B, Nielsen FG. Modeling, simulation and control of a wind turbine with a hydraulic transmission system. *Wind Energy*. 2013;16(8):1259-1276.
18. Laguna AJ. Modeling and analysis of an offshore wind turbine with fluid power transmission for centralized electricity generation. *J Comput Nonlinear Dyn*. 2015;10(4):041002.
19. Wright AD, Fingersh L. Advanced control design for wind turbines; Part I: Control design, implementation, and initial tests. tech. rep., Golden, CO (United States), National Renewable Energy Lab.(NREL); 2008.
20. Hou Z, Jin S. A novel data-driven control approach for a class of discrete-time nonlinear systems. *IEEE Trans Control Syst Technol*. 2011;19(6):1549-1558.
21. Lu C, Zhao Y, Men K, Tu L, Han Y. Wide-area power system stabiliser based on model-free adaptive control. *IET Control Theory Appl*. 2015; 9(13):1996-2007.
22. Zhang H, Zhou J, Sun Q, Guerrero JM, Ma Ds. Data-driven control for interlinked AC/DC microgrids via model-free adaptive control and dual-droop control. *IEEE Trans Smart Grid*. 2017;8(2):557-571.
23. Lu X, Li W, Lin Y. Load control of wind turbine based on model-free adaptive controller. *Trans Chinese Soc Agric Mach*. 2011;10:109-119.
24. Jonkman JM, Buhl MLBJr. Fast user's guide. *tech. rep*. No NREL/EL-500-38230, Golden, CO, National Renewable Energy Laboratory; 2005.
25. Singh M, Muljadi E, Jonkman J, Gevorgian V, Girsang I, Dhupia J. Simulation for wind turbine generators with FAST and MATLAB-simulink modules. *tech. rep*. No NREL/TP-5D00-59195, Golden, CO, National Renewable Energy Laboratory; 2014.
26. Mäkinen J, Pertola P, Marjamaki H. Modeling coupled hydraulic-driven multibody systems using finite element method. In: 1st Joint International Conference on Multibody System Dynamics Lappeenranta University of Technology; 2010; Lappeenranta, Finland:1326–1335.
27. Mäkinen J, Piche R, Ellman A. Fluid transmission line modeling using a variational method. *J Dyn Syst Meas Control*. 2000;122(1):153-162.
28. Dutta R, Wang F, Bohlmann BF, Stelson KA. Analysis of short-term energy storage for midsize hydrostatic wind turbine. *J Dyn Syst Meas Control*. 2014;136(1):011007.
29. Hou Z, Chi R, Gao H. An overview of dynamic-linearization-based data-driven control and applications. *IEEE Trans Ind Electron*. 2017;64(5):4076-4090.
30. Hou Z, Jin S. Data-driven model-free adaptive control for a class of MIMO nonlinear discrete-time systems. *IEEE Trans Neural Netw*. 2011;22(12):2173-2188.
31. Hou Z, Jin S. *Model Free Adaptive Control: Theory and Applications*. CRC press: Boca Raton, USA; 2013.

32. Mathwork. Control system toolbox reference. Available online: https://www.mathworks.com/help/pdf_doc/control/reference.pdf; retrieved on 21/04/2019; R2019a.
33. Liu Y, Anderson BD. Singular perturbation approximation of balanced systems. *Int J Control*. 1989;50(4):1379-1405.
34. Gu DW, Petkov P, Konstantinov MM. *Robust Control Design with MATLAB®*. London, United Kingdom: Springer; 2005.
35. Varga A. Balancing free square-root algorithm for computing singular perturbation approximations. In: Proceedings of the 30th IEEE Conference on Decision and Control IEEE; 1991:1062-1065.
36. Le V, Safonov M. Rational matrix GCDs and the design of squaring-down compensators – a state-space theory. *IEEE Trans Autom Control*. 1992;37(3):384-392.
37. Glover K, McFarlane D. Robust stabilization of normalized coprime factor plant descriptions with H_∞-bounded uncertainty. *IEEE Trans Autom Control*. 1989;34(8):821-830.
38. Doyle JC. Lecture notes in advances in multivariable control. In: ONR/Honeywell Workshop. Minneapolis, USA; 1984.
39. MeFarlane D, Glover K. A loop shaping design procedure using H_∞ synthesis. *IEEE Trans Autom Control*. 1992;37(6):759-769.
40. Vidyasagar M, Kimura H. Robust controllers for uncertain linear multivariable systems. *Automatica*. 1986;22(1):85-94.
41. Balas G, Chiang R, Packard A, Safonov M. Robust control toolbox reference. Available online: https://www.mathworks.com/help/pdf_doc/robust/robust_ref.pdf; retrieved on 21/04/2019; R2019a.
42. Commission IE. Wind turbine generator systems—part 1: Safety requirements, 2nd ed. IEC 61400-1 tech. rep., Geneva, Switzerland, International Electrotechnical Commission; 1999.
43. Commission IE. Wind turbine generator systems—part 1: Safety requirements, 3rd ed. tech. rep., JIS C1400-1-2001, Geneva, Switzerland, International Electrotechnical Commission; 2005.
44. Jonkman BJ. Turbsim user's guide: Version 1.50. tech. rep., NREL/TP-500-46198, CO USA, National Renewable Energy Laboratory; 2009.
45. Jonkman JM, Buhl MLJr. Loads analysis of a floating offshore wind turbine using fully coupled simulation. tech. rep., NREL/CP-500-41714, Golden, CO (United States), National Renewable Energy Lab. (NREL); 2007.
46. Hayman GJ. MLife user's guide for version 1.00. tech. rep., NREL/TP-XXXXX, Golden, CO, National Renewable Energy Laboratory (NREL); 2012.
47. Hayman GJ. MLife theory manual for version 1.00. tech. rep., NREL/TP-XXXXX, Golden, CO, National Renewable Energy Laboratory (NREL); 2012.

How to cite this article: Lin S, Qi P, Zhao X. Power generation control of a hydrostatic wind turbine implemented by model-free adaptive control scheme. *Wind Energy*. 2020;23:849-863. https://doi.org/10.1002/we.2437